Surface & Coatings Technology 205 (2010) 1969–1978

Contents lists available at ScienceDirect

Surface & Coatings Technology

journal homepage: www.elsevier.com/locate/surfcoat

Electroplating and characterization of Zn–Ni, Zn–Co and Zn–Ni–Co alloys

N. Eliaz [a,*], K. Venkatakrishna [b], A. Chitharanjan Hegde [b,*,1]

[a] Materials and Nanotechnologies Program & School of Mechanical Engineering, Tel-Aviv University, Ramat-Aviv, Tel-Aviv 69978, Israel
[b] Department of Chemistry, National Institute of Technology Karnataka, Srinivasnagar 575 025, India

ARTICLE INFO

Article history:
Received 2 February 2010
Accepted in revised form 19 August 2010
Available online 25 August 2010

Keywords:
Zn-based alloys
Electrodeposition
Anomalous codeposition (ACD)
Corrosion resistance

ABSTRACT

Zn–Ni, Zn–Co and Zn–Ni–Co coatings were electrodeposited on mild steel from an acidic chloride bath containing *p*-aminobenzenesulphonic acid (SA) and gelatin. These additives changed the phase content in the coatings, most likely as a result of their adsorption at the surface of the cathode. The effect of gelatin was more pronounced than that of SA. The Faradaic efficiency was higher than 90%. As the current density was increased or the bath temperature was decreased, the concentration of the nobler metal in the coating increased. Both concentrations of Ni and Co in the ternary alloy increased as the applied current density was increased. Nickel and cobalt were found to have a synergistic catalytic effect. The thickness of all coatings increased as the applied current density was increased. The hardness increased with current density to a peak value, and then decreased. The rate of Zn deposition was heavily influenced by mass-transport limitation at high applied current densities, while the rates of Ni and Co deposition were not. The anomalous codeposition was explained by the great difference between the exchange current densities of Zn and the iron-group metal. Potentiodynamic polarization scans and electrochemical impedance spectroscopy showed that the corrosion resistance of the ternary Zn–Ni–Co alloy coatings was approximately 10 times higher than that of Zn–Ni and 7 times higher than that of Zn–Co. The improved corrosion resistance of the ternary alloy was attributed to its surface chemistry, phase content, texture, and surface morphology. The ternary Zn–Ni–Co coating may thus replace the conventional Zn–Ni and Zn–Co coatings in a variety of applications.

1. Introduction

Electroplating of metals and alloys has become widely used in many industries, with distinct advantages compared to most other coating technologies [1]. Electroplated binary Zn–M alloys, where M is an iron-group metal (Fe, Co or Ni), exhibit improved properties compared to pure Zn [2,3]. Zn–Ni coatings have been formed by DC plating [4–14], pulse plating [15], and as composition modulated alloys (CMA's) [16]. Zn–Co coatings have also been formed by DC plating [6,7,17,18], pulse plating [19], and as CMA's [20,21].

The corrosion resistance of Zn–M alloys has been found to depend significantly on the concentration of M in the deposit [22]. The use of specific bath additives has also been found beneficial with respect to corrosion resistance, even for low contents of M [23]. It has been observed that the ternary alloy Zn–Ni–Co is characterized by enhanced corrosion resistance compared to the binary Zn–Ni and Zn–Co alloys [24–27].

The term anomalous codeposition (ACD) was coined by Abner Brenner [28] to describe an electrochemical deposition process in which the less noble metal is deposited preferentially under most plating conditions. This behavior is typically observed in codeposition of iron-group metals, or in codeposition of an iron-group metal with Zn or Cd. In the deposition of Ni–Zn alloys, for example, adding either ion to the solution enhances the rate of deposition of the other metal [1]. Several models have been suggested to explain the ACD of Zn–M alloys [20,29–37]. Other behaviors have been reported by Eliaz et al. for electroplating of Ni–W [38,39] or Re–M [40,41] alloys.

The present work was aimed at comparative evaluation of Zn–Ni, Zn–Co and Zn–Ni–Co coatings, with emphasis on surface morphology, chemistry, phase content, and corrosion resistance. In addition, possible mechanisms for ACD in the studied systems were sought.

2. Experimental

Acidic baths consisted of $ZnCl_2$, $NiCl_2$, $CoCl_2$, sulphanilic acid (SA, $NH_2C_6H_4SO_3H$, IUPAC name: *p*-aminobenzenesulphonic acid) and gelatin were used (see Table 1). SA has a relatively high melting point (288 °C) and moderate solubility in water (>20 g L^{-1} at 25 °C). The authors are not aware of any other paper where SA was one of the constituents of an electroplating bath for either binary or ternary Zn-based alloy. We observed that SA improved the brightness and uniformity of coatings. Fourier transform infrared spectroscopy

* Corresponding authors. Eliaz is to be contacted at Tel.: +972 3 6407384; fax: +972 3 6407617. Hegde, Tel.: +91 824 2474000; fax: +91 824 2474033.
E-mail addresses: neliaz@eng.tau.ac.il (N. Eliaz), achegde@rediffmail.com (A.C. Hegde).
[1] A.C. Hegde conducted some of the work at Tel-Aviv University.

0257-8972/$ – see front matter © 2010 Elsevier B.V. All rights reserved.
doi:10.1016/j.surfcoat.2010.08.077

Table 1
Composition and operating conditions optimized baths for electroplating of bright Zn–Ni, Zn–Co and Zn–Ni–Co alloys on mild steel.

Concentration	Zn–Ni bath	Zn–Co bath	Zn–Ni–Co bath
$ZnCl_2$ (M)	0.37	0.29	0.37
$NiCl_2$ (M)	0.34	–	0.34
$CoCl_2$ (M)	–	0.04	0.04
NH_4Cl (M)	2.24	2.24	2.24
KCl (M)	1.61	1.48	1.61
$C_6H_7NO_3S$ (M)	0.03	0.06	0.03
Gelatin (g L^{-1})	7	5	7
pH	3.5	3.5	3.5
T (°C)	30	30	30
i (mA cm^{-2})	30	20	40

revealed the presence of S–O and N–H groups in the coating. Thus, it was puzzling whether SA acted as a brightener only, or also as a complexing agent (the latter was more likely in Co-containing baths, where its concentration was similar to that of the Co ion concentration). Gelatin is a hydrolyzed form of collagen, which is sometimes added to electroplating baths (e.g., in zinc electrodeposition [42]) to control the deposition rate, crystallization, leveling and brightness of the deposit. Due to its very high molecular weight, its content in the plating baths in the present study represents concentrations which were several orders of magnitude smaller than the concentrations of the zinc and iron-group metal ions. Thus, gelatin could not act as a complexing agent. NH_4Cl and KCl were added to increase the conductivity and ionic strength of the electrolyte. At the pH of the baths in this study (3.5), ammonia exists in solution entirely as NH_4^+ species [1], thus the possible act of NH_3 as a complexing agent can be excluded. The plating solutions were freshly prepared from distilled water and analytical grade reagents.

Electroplating of mild steel plates was done at pH 3.5 ± 0.05 and 30 ± 2 °C for either 10 min or 20 min. The pH was lowered from its initial value (3.5–4.0) to 3.5, by adding dilute HCl, because pH 3.5 was found to yield the best coatings for the same bath composition and temperature. The polished steel plates had an exposed surface area of either 7.5 cm^2 or 25 cm^2 and served as a cathode. The anode was pure Zn with the same exposed area. A rectangular PVC cell containing 250 cm^3 electrolyte solution was used, in conjunction with an adjustable power source. All depositions were carried out under identical stirring condition in order to maintain similar mass transport conditions near the cathode. No nitrogen (or other) purging was applied. The bath composition and operating conditions for deposition of Zn–Ni, Zn–Co and Zn–Ni–Co coatings were optimized by means of a standard Hull cell. The effect of each bath constituent on the appearance of the coating on a Hull cell panel was examined. While varying the concentration of one constituent in constant increments, the concentrations of all other constituents were kept constant. The concentration of a specific constituent at which the bath produced a bright, homogeneous coating, which was not peeled-off in a tape test, was fixed as its 'optimal' concentration. The procedure was repeated for all constituents, limiting the applied current density to within 10–60 mA cm^{-2}, which yielded deposits with different appearances (gray/white/black, bright/semi-bright, porous/powdery). Obviously, as the overpotential is different for each metal, the partial current density (kinetics) for each metal is expected to be different too. The effect of bath chemistry on the appearance and surface morphology of the coatings was evaluated. The composition and operating conditions of optimized baths are given in Table 1. It is worth noting that the use of a much lower concentration of Co than Ni and Zn is typical for Co-containing baths [25] and was found to yield brighter and smoother coatings in this study.

The effect of Co-content on the appearance and corrosion resistance of the ternary alloy was studied. The Faradaic efficiency (FE) was calculated from the mass gained, the charge passed and the chemical composition of the deposit:

$$FE = \frac{\text{measured mass gain}}{\text{theoretical mass gain}} \times 100 = \frac{w}{\frac{EW \times I \times t}{F}} \times 100 = \frac{wF}{It} \sum \frac{c_i n_i}{M_i} \times 100 \quad (1)$$

where w is the measured mass of the deposit (g), t is the deposition time (s), I is the average applied current (A), EW is the equivalent weight of the alloy (g $equiv^{-1}$), c_i is the weight fraction of the element in the alloy deposit, n_i is the number of electrons transferred per atom of each metal, M_i is the atomic mass of that element and F is the Faraday's constant (96,485 C mol^{-1}). While the thickness of the coating was estimated by Faraday's law, it was verified by measurements, using a digital thickness meter (Coatmeasure model M & C). The partial deposition current densities were calculated from the mass gained and the chemical composition of the deposit, using the equation:

$$i_i = \frac{w}{At} \times \frac{c_i n_i F}{M_i} \quad (2)$$

where i_i is the partial current density of element i (A cm^{-2}) and A is the surface area of the cathode (cm^2).

Cyclic voltammetry (CV) was performed in a conventional three-electrode cell in order to better understand the process of electrodeposition in each of the three systems and to identify the effects of bath additives (namely, gelatin and SA). The bath composition was as in Table 1. All chemicals used were of analytical grade. Double distilled water was used for preparation of the electrolyte solutions. Before carrying out the experiments, the pH of the solution was brought to 3.5 and the bath temperature was stabilized at 30 °C. Pure platinum foil with a surface area of 1 cm^2 was used as working electrode. Although this is a different material than the steel substrate used for galvanostatic deposition, it enabled elimination of noise in the CV experiments. Furthermore, it may be argued that once several nanometers of coating material are deposited, the substrate no longer has any effect on the deposition process. Before each experiment, the electrode was activated by immersion in dilute HNO_3. The CV experiments were conducted in a quiescent solution, without purging. Initially, three scan rates were evaluated: 10, 20 and 50 mV s^{-1}. However, the peaks in the CV spectra became more distinct at 10 mV s^{-1}, thus this scan rate was further used. The scan began from 0 V in the positive direction, up to +1.0 V. Then, the scan was reversed to the negative direction, down to −1.4 V, and finally reversed back to +1.0 V. The potentials were measured versus a saturated calomel reference electrode (SCE). Although, in some cases, the use of a fixed negative vertex potential might prevent determination that the potential or time modified the structure of the deposit, this was not a concern in this study because Zn was found to be dominant in the deposition of all three coating systems (see, for example, Table 5).

The aqueous corrosion behavior of the coatings was studied by the potentiodynamic polarization and electrochemical impedance spectroscopy (EIS) techniques. The corrosion current density and corrosion potential were determined based on Tafel's extrapolation. The exposed surface area of all samples was 1 cm^2. A standard three-electrode cell containing 5% analytical grade sodium chloride (NaCl) at 25 °C was used. The potential was measured versus SCE, whereas Pt mesh was used as a counter electrode. An Electrochemical Work Station (PGSTAT 30 from Metrohm) was used and applied a scan rate of 1 mV s^{-1}, from −0.5 V *vs.* open-circuit potential (OCP) to +1.0 V *vs.* OCP. The EIS measurements were run from 100 kHz to 10 mHz, and the Nyquist plots were analyzed.

Characterization of the coatings was done by a variety of analytical facilities. The surface morphology of the deposits was observed by means of an environmental scanning electron microscope (ESEM, Quanta 200 FEG from FEI). The attached liquid-nitrogen-cooled Oxford

Si energy dispersive spectroscopy (EDS) detector was used to determine the atomic composition of the alloy. Each sample was analyzed at five locations, to confirm uniformity. The composition of the alloys was also measured by stripping the deposit into dilute HCl solutions followed by colorimetric analysis [43]. X-ray Photoelectron Spectroscopy (XPS) measurements were performed in UHV (2.5×10^{-10} Torr base pressure), using a 5600 Multi-Technique System (PHI, USA). The samples were irradiated with an Al–K_α monochromated source (1486.6 eV), and the emitted electrons were analyzed by a spherical capacitor analyzer, using a slit aperture of 0.8 mm in diameter. Analysis was made at the surface as well as after sputter cleaning with 4 kV Ar^+ ion gun. Charging was compensated with charge neutralizer. The binding energy (BE) of adventitious carbon at 285 eV was taken as an energy reference for the measured peaks. A low-resolution survey spectrum was taken over a wide energy range (0–1400 eV), in order to identify the elements present at the sample surface. High-resolution spectra were then acquired at pass energy of 23.5 eV, at an increment of 0.05 eV $step^{-1}$. Finally, the hardness of the deposited alloys was measured using a computer-controlled micro-hardness tester (model MMT-X7 from Clemex) and the Vickers test.

3. Results and discussion

3.1. The role of gelatin and SA

The standard potentials of Zn, Ni and Co are –0.76, –0.25 and –0.28 V vs. SHE, respectively. Therefore, according to the Nernst equation, the reversible potentials for deposition of these metals at 30 °C, for their respective ion concentrations as in Table 1, are –1.02, –0.50 and –0.53 V vs. SCE, respectively. These values neglect the activity coefficient of the ions. Moreover, in the presence of a ligand, a shift in the deposition potential is expected. It should also be born in mind that while the hydrogen evolution reaction proceeds very slowly on Zn, it is faster (i.e. a much higher exchange current density) on Ni and Co. Underpotential deposition of Zn on ferrous substrates, for example, has been claimed to compete with the proton reduction [31].

Fig. 1a shows cyclic voltammograms obtained in the Zn–Ni system on Pt electrode. Without additives, the deposition Zn(II)→Zn(0) started at approximately –1.15 V, while hydrogen evolution was indicated by c2. Previous studies have shown that the zinc reduction process is controlled by mass transport [44]. The detection of multiple peaks during the electrochemical oxidation of alloys has been attributed to the sequential oxidation of different phases [45]. Accordingly, the anodic sweep in Fig. 1a showed a shoulder a'1 and two dissolution peaks—a2 related to Zn dissolution from a Zn–Ni phase, and a1 related to the dissolution of the porous Ni matrix left after the preferential dissolution of Zn from the Zn-rich phases. In electrodeposited systems, the phases formed are often not in thermodynamic equilibrium, and may be either undersaturated or oversaturated compared to their counterparts in the equilibrium phase diagram. Electrodeposited Zn–Ni alloys have been reported to contain three major phases: the η phase (a solid solution of Ni in Zn with a hexagonal crystal structure, containing up to 1 at.% Ni), the γ phase (an intermetallic compound Ni_5Zn_{21} with a bcc structure), and the α phase (a solid solution of Zn in Ni with a fcc structure, containing up to 40 at.% Zn) [11,29,46–48]. The variables that determine the phase composition are the Ni/Zn ratio in the electrolyte, the applied current density, bath temperature, and agitation [48]. Swathirajan [29] has shown that Zn exhibits equilibrium potentials of –1.00, –0.94 and –0.67 V vs. SCE when present in the η, γ and α phases, respectively, deposited from a chloride bath with Ni/Zn = 5.0. Hence, peak a2 in Fig. 1a may be attributed to the α phase [29,48]. In Fig. 1a it is also evident that when the scan was reversed at –1.4 V, two crossovers appeared, known as the nucleation overpotential (E_η) and the crossover potential (E_{co}). The appearance of these two crossovers is characteristic of processes that involve the

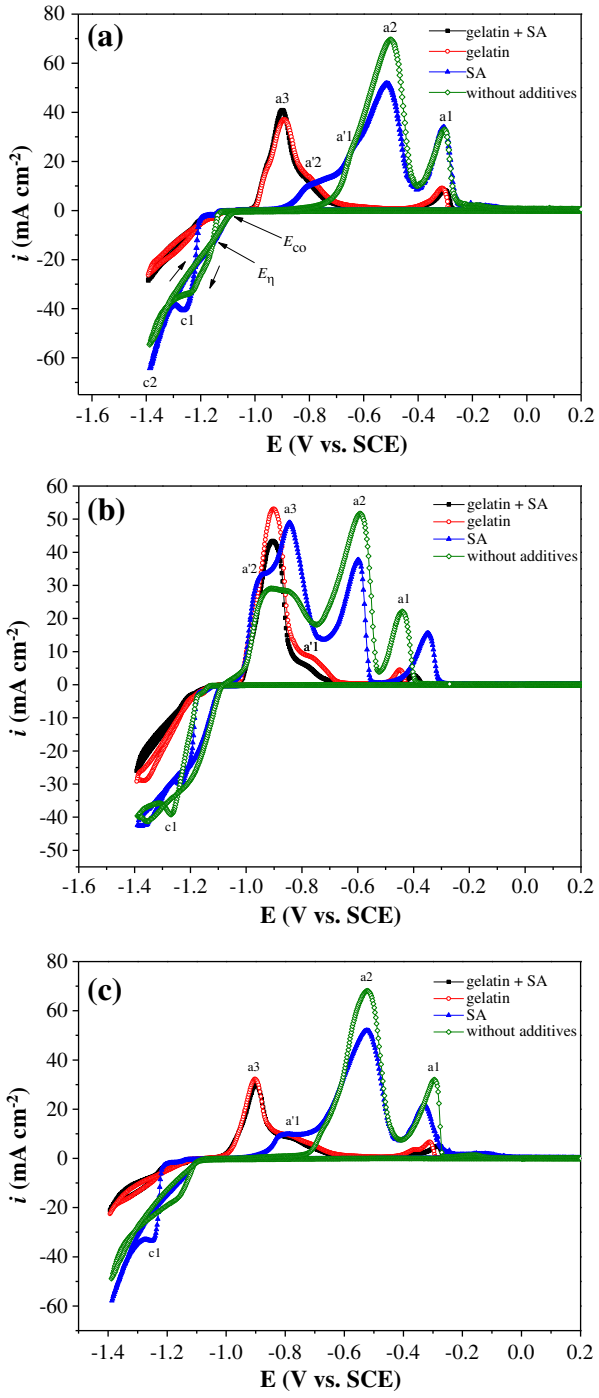

Fig. 1. Cyclic voltammograms for (a) Zn–Ni, (b) Zn–Co, and (c) Zn–Ni–Co baths, demonstrating the effects of gelatin and SA. Working electrode: Pt, pH = 3.5, T = 30 °C, υ = 10 mV s^{-1}.

nucleation of a new phase [44]. The addition of SA shifted the deposition potential in the negative direction, starting at around –1.21 V, and made the peak c1 more distinct, thus reflecting an increase in the FE. The displacement of c1 to a more negative value due to the presence of SA represents cathodic polarization, and may be related to the adsorption of SA onto the Pt surface. The overpotential associated with peak c1 can be determined as $\eta = E_{c1} - E_{co}$ [44,49]. Hence, we obtain that this overpotential increased from –0.16 V to –0.19 V due to the addition of SA. This finding suggests that SA acts as a barrier for discharge of metal ions at the interface. In the anodic sweep, a shoulder a'2 appeared at –0.8 V, while the area (charge) below a2

decreased, thus possibly reflecting the presence (and dissolution) of a second Zn-rich phase. The presence of gelatin changed the shape of the voltammograms in two ways: (i) the deposition potential was shifted to slightly less negative value (starting at around −1.13 V) while the deposition current density was decreased, and (ii) the intensity of a1 was reduced, a2 disappeared, and a new peak (a3) appeared at −0.89 V, jointly with a shoulder a'2. The peak a3 may be related to the η and γ phases [29,48]. Thus, the presence of gelatin in the bath resulted in a change in the phase content in the alloy coating. As explained in Section 2, its low concentration in the bath should prevent it from acting as a complexing agent. Thus, it seems that gelatin affected the deposition process through preferential adsorption on the surface of the cathode. As evident in Fig. 1a, the effect of gelatin was more pronounced than that of SA in the bath containing both of these additives.

In the case of the Zn–Co system (Fig. 1b) without additives, the deposition (peak c1) started at around −1.18 V, similar to that of Zn–Ni. Hence, it seems that the deposition potential was dictated mainly by Zn. In the anodic sweep, the Zn–Co system differed from Zn–Ni, revealing three peaks. The broad peak at −0.9 V (between a'2 and a3) may be related to dissolution of pure Zn and/or Zn from the η phase (a solid solution of Co in Zn with a hcp structure) [50]. Peak a2 at −0.59 V may be attributed to dissolution of Zn from the γ phase (Co_5Zn_{21} with a bcc structure) [50]. Peak a1 at −0.44 V may be related to dissolution of the porous Co matrix left after the preferential dissolution of Zn from the γ phase. When SA was added, the deposition started at around −1.18 V. The first oxidation peak deconvolved into a shoulder a'2 and a peak a3 at −0.85 V. While the peak a2 remained at nearly −0.59 V, peak a1 was shifted to −0.35 V (possibly indicating dissolution of pure Co). The presence of SA increased the intensity of a'2-a3 compared to a2 and a1, thus indicating that the addition of SA to the bath resulted in a higher content of the Zn-rich phase in the alloy coating. The presence of gelatin in the bath changed the appearance of the voltammograms significantly. When it was the only additive in the bath, the deposition potential was shifted to −1.16 V and the deposition current density was reduced. A similar deposition potential was apparent when both gelatin and SA were present. In the anodic sweep, a shoulder a'1 appeared, while peak a2 disappeared. Peak a1 was at −0.45 V when only gelatin was present, and at −0.40 V when both gelatin and SA were present. The changes in the peak intensities in Fig. 1b indicate that when gelatin was added to the bath, the coatings became richer in Zn. As in Fig. 1a, the effect of gelatin was more pronounced than that of SA in the bath containing both of these additives.

Fig. 1c shows the cyclic voltammogram obtained for Zn–Ni–Co bath. This voltammogram is similar to that of Zn–Ni (Fig. 1a) than to that of Zn–Co (Fig. 1b). Without any additives, the deposition potential was at around −1.17 V. Two oxidation peaks appeared: a2 at −0.52 V (may be related to the α phase), and a1 at −0.29 V (may be related to dissolution of porous Ni or Co). The addition of SA shifted the deposition potential to −1.25 V, thus representing cathodic polarization. The overpotential consequently increased from −0.05 V to −0.17 V. An anodic shoulder a'1 appeared at around −0.82 V. The intensities of peaks a2 and a1 were reduced, while peak a1 was also shifted to a more negative potential. The presence of gelatin changed the behavior in this system too. The deposition potential was around −1.15 V. An oxidation peak a3, which may be attributed to the η and γ phases, appeared at −0.90 V. A doublet peak appeared at −0.36 V and −0.31 V when gelatin was the only additive. In combination with SA, an oxidation peak appeared at −0.28 V.

3.2. The effect of current density on the Faradaic efficiency, appearance and chemical composition of the coating

Both Zn–Ni and Zn–Co baths produced semi-bright deposits at low current density and porous bright deposits at high current density. The effects of the applied current density on the *FE* and the chemical composition of Zn–Ni, Zn–Co and Zn–Ni–Co alloys are shown in Fig. 2a,b,c, respectively. The mass gain measured in each case is listed in Tables 2, 3 and 4, respectively. In all cases, the *FE* was high (namely, higher than 90%). The dependence of the *FE* on the applied current density was different in each of the three alloy systems. In general, while a decrease in *FE* with increasing current density could lead to improved thickness uniformity of a plating, an increase in *FE* with

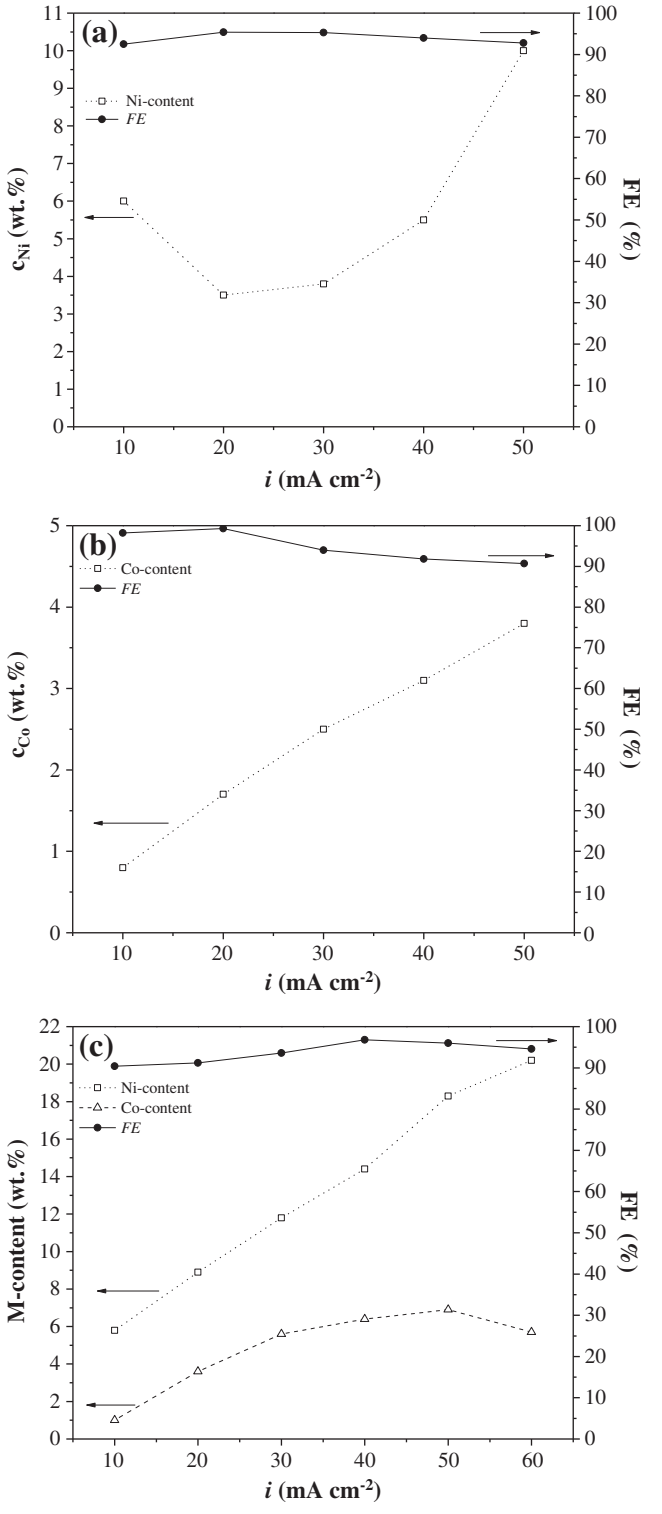

Fig. 2. The dependence of Faradaic efficiency (solid symbols, solid lines) and the iron-group metal content of the deposit (empty symbols, dot lines) on current density. Plating was conducted for 20 min at pH = 3.5 and T = 30 °C on steel with an exposed area of 25 cm^2. (a) Zn–Ni, (b) Zn–Co, and (c) Zn–Ni–Co.

Table 2
The effects of applied current density on the mass gain, thickness and hardness of the Zn–Ni coatings, as well as on their corrosion characteristics.

i (mA cm^{-2})	w (mg)	VHN	t (μm)	E_{corr} (–V *vs.* SCE)	i_{corr} (μA cm^{-2})	CR (μm y^{-1})
10	93.2	172	7.6	1.063	39.5	567
20	193.1	197	15.9	1.083	31.7	455
30	289.6	220	20.5	1.142	14.9	214
40	379.8	214	25.0	1.097	18.0	258
50	467.7	205	27.8	1.089	36.4	522

increasing current density could lead to rapid roughening of the surface [1].

In all three systems, as the current density was increased, the concentration of the nobler (iron-group) metal in the coating increased too (Fig. 2). It is assumed here that the composition of the coating is governed by complexes of the iron-group metal, the stability of which is pH dependent. Other researchers too have reported an increase in the content of the nobler metal in the coating when the applied current density was increased [51–53]. In the case of the Zn–Ni system, the composition at $i = 10$ mA cm^{-2} seems to behave differently. However, there is no solid reason to assume that this is associated with a transition to non-anomalous codeposition at low current densities, such as that reported for Zn–M systems [28,30,32,33,36]. Comparing between the binary alloy systems, at each current density the concentration of Ni in the coating was higher than that of Co. As both the atomic masses and the standard potentials of the two elements are similar, the higher concentration of Ni in the coating compared to Co may be associated with the higher concentration of the former ion in solution. Both concentrations of Ni and Co in the ternary alloy increased as the current density was increased. Moreover, for each current density, the concentration of each element in the ternary alloy was higher than its corresponding concentration in the binary alloy. This means that there could be a synergistic catalytic effect (rather than an inhibitory effect), due to their co-presence in solution.

Fig. 3 shows the dependence of the partial current densities of Zn, Ni and Co on the applied current density. It is evident that in all cases, the partial current densities increased as the applied current density was increased. It is also evident that in all three alloy systems the partial current density of Zn is always higher than those of the iron-group metals. The partial current density of Zn in the case of the ternary alloy decreased compared to that in the case of the binary alloys, whereas the partial current densities of the iron-group metals increased. This supports the possibility of a synergistic catalytic effect of Ni on Co and vice versa. Dividing the sum of the partial current densities of Zn, Ni and Co by the applied current density resulted in values essentially identical to those of the *FE* shown in Fig. 2. It is assumed that the partial current density of the hydrogen evolution reaction would complement this ratio to nearly 100%.

3.3. The effect of bath temperature

In this work it was observed that the content of the iron-group metal in the coating decreased as the bath temperature was increased

Table 3
The effects of applied current density on the mass gain, thickness and hardness of the Zn–Co coatings, as well as on their corrosion characteristics.

i (mA cm^{-2})	w (mg)	VHN	t (μm)	E_{corr} (–V *vs.* SCE)	i_{corr} (μA cm^{-2})	CR (μm y^{-1})
10	99.7	150	5.4	1.119	32.3	467
20	201.5	160	10.5	1.081	9.5	138
30	283.9	175	15.5	1.129	9.4	148
40	369.4	180	20.2	1.119	15.8	229
50	459.1	160	24.9	1.106	28.2	408

Table 4
The effects of applied current density on the mass gain, thickness and hardness of the Zn–Ni–Co coatings, as well as on their corrosion characteristics.

i (mA cm^{-2})	w (mg)	VHN	t (μm)	E_{corr} (–V *vs.* SCE)	i_{corr} (μA cm^{-2})	CR (μm y^{-1})
10	91.2	146	8.6	1.259	14.7	212
20	182.8	164	13.6	0.773	3.0	43
30	280.0	186	18.4	0.702	2.2	31
40	384.5	204	22.2	0.687	1.4	20
50	474.3	218	26.8	0.736	1.9	28
60	560.5	214	30.4	0.837	2.8	41

in all three systems. This behavior indicates that the electrodeposition in this study is, at least partially, mass transport controlled (which is more likely at high current densities). Brenner [28] noted that, as the bath temperature is increased, cathodic polarization would favor a decrease while diffusion would favor an increase in the content of the less noble metal (Zn). Nevertheless, it should be born in mind that the enthalpy of activation for a diffusion-controlled processes is usually smaller than for common chemical reactions (~12–20 versus 40–100 kJ mol^{-1}, respectively). Consequently, at high temperatures the rate constant k would be more dominant than the diffusion coefficient D. Therefore, it is probable that the temperature affects either the distribution of complexes of the iron-group metals (either with SA or with gelatin) or, more likely based on other results obtained in this study—the adsorption of gelatin on the surface of the cathode.

In order to determine how far the actual partial deposition current densities of Zn, Ni and Co were from the respective limiting current densities (i.e. whether mass-transport limitation conditions prevailed), the following experiment was conducted. Potentiodynamic polarization scans were used to determine the limiting current density i_L of each metal separately, under exactly the same conditions of cell configuration, area of electrodes and stirring, but at a concentration that was 10 times lower than the actual concentration listed in Table 1 (in order to eliminate the effect of dendrite formation as the applied current density approaches i_L). The measured i_L value was then multiplied by 10, to obtain the actual i_L during deposition. Thus, i_L values of 39.8, 42.8 and 9.5 mA cm^{-2} were measured for Zn, Ni and Co, respectively. The measured values are similar to the ones calculated using the relation:

$$i_L = \frac{nFDc}{\delta} \tag{3}$$

where $n = 2$ equiv mol^{-1}, δ is the Nernst diffusion layer thickness ($\approx$0.01 cm under stirred conditions), and D is the diffusivity of the ion in solution (taken as 7×10^{-6} cm^2 s^{-1} for Zn^{2+}, Ni^{2+} and Co^{2+}). The

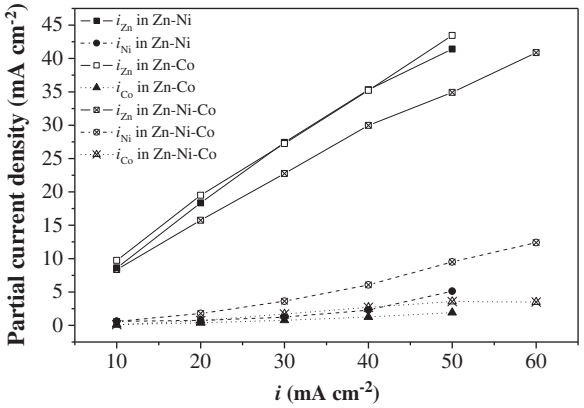

Fig. 3. The dependence of the partial current densities of Zn, Ni and Co on the applied current density. Plating was conducted for 20 min at pH = 3.5 and $T = 30$ °C on steel with an exposed area of 25 cm^2.

calculated i_L values are thus 39.2/50 (depending on the bath composition), 45.9 and 5.4 mA cm^{-2} for Zn, Ni and Co, respectively.

Next, the partial deposition current densities (Fig. 3) were divided by the respective limiting current densities. Thus, for the Zn–Ni system, it was found the $i_{Zn}/i_{L,Zn}$ increased from 0.22 to 1.0, while $i_{Ni}/i_{L,Ni}$ increased from 0.01 to 0.12, as the applied current density was raised from 10 to 50 mA cm^{-2}. Similarly, in the case of the Zn–Co system, $i_{Zn}/i_{L,Zn}$ increased from 0.24 to 1.0, while $i_{Co}/i_{L,Co}$ increased from 0.01 to 0.20, as the applied current density was raised from 10 to 50 mA cm^{-2}. In the case of the Zn–Ni–Co system, $i_{Zn}/i_{L,Zn}$ increased from 0.21 to 0.88, while $i_{Ni}/i_{L,Ni}$ increased from 0.01 to 0.22 and $i_{Co}/i_{L,Co}$ increased from 0.01 to 0.38, as the applied current density was raised from 10 to 50 mA cm^{-2}. These results show that, in all cases, the rate of Zn deposition was heavily influenced by mass-transport limitation at high applied current densities, while the rates of Ni and Co deposition were not.

3.4. The essence of anomalous codeposition and its possible mechanism

The high concentrations of the less noble metal (Zn) in the coatings reflect anomalous codeposition (ACD). It should be noted that the Zn/M ion ratio in the bath solution was 1.09, 7.25 and 0.97 in the case of Zn–Ni, Zn–Co and Zn–Ni–Co systems, respectively (i.e. always much lower than the corresponding ratio between elements in the coating).

Several models have been proposed to explain the ACD of Zn–M alloys. *One model* suggests that, due to hydrogen evolution and the resulting pH increase, a zinc hydroxide film precipitates and adsorbs on the surface of the cathode. As the critical pH for precipitation of iron-group metal hydroxides is significantly higher than for precipitation of zinc hydroxide, the former may not form so that M-deposition requires direct discharge of M^{2+} ions through the zinc hydroxide film. At sufficiently high current densities, the high resistance of this hydroxide film favors Zn reduction while inhibiting M-deposition. This model is often termed the Hydroxide Suppression Mechanism [30,32,33,35]. It has been supported by measurement of an abrupt pH increase in vicinity of the cathode [33] as well as by electrochemical quartz crystal microbalance (EQCM) measurements [37]. However, as the XPS and XRD data in this study (Sections 3.7 and 3.8, respectively) did not indicate the presence of zinc hydroxide, it is believed that this model is not applicable to our study. A *second model* suggests that the formation of trivalent cobalt ions Co^{3+} in solution by oxidation of Co^{2+} ions prevented the formation of Co-rich Zn–Co alloys [20]. However, as the standard potential for the reduction reaction Co^{3+}/Co^{2+} (+1.92 V *vs.* SHE [54]) is much higher than the deposition potentials of both Co and Zn, this could not be a likely explanation. A *third model* suggests that underpotential deposition (UPD) of Zn provides an alloy surface that is different from the parent metal for the continuous codeposition, thus making the deposition of the less noble component preferable [30,37]. However, if this was the case, once a monolayer is deposited, the UPD should be terminated and the ions in solution should "sense" only the last layer deposited on the surface. Hence, such a model is valid only if an alternating multilayer coating is formed, which was not the case in this study. According to a *fourth model*, the great difference between the exchange current densities of Zn and the iron-group metal results in a significant difference between the thermodynamic and the practical nobility. In this regard, the magnitude of the exchange current density is generally much greater for Zn compared to Ni, Co and Fe [30,31,34,35]. We believe that *this is the only model among the models already suggested in the literature that is applicable in our study*. It should be born in mind that such a model may be proper for electroplating under galvanostatic conditions (as in our study), where a high current consumption by one element must be at the expense of another element, but may not be applicable to electroplating under potentiostatic conditions.

3.5. The thickness, hardness and roughness of coatings

The thickness of all alloy coating systems was found to increase as the applied current density was increased (see Tables 2–4). Such a thickness increase is expected when the *FE* is essentially constant. The hardness, on the other hand, increased with current density to a peak value and then decreased (Tables 2–4). The peak hardness of the Zn–Ni and Zn–Ni–Co alloys was similar, and slightly higher than that of Zn–Co. The mean roughness R_a was determined based on atomic force microscope (AFM) images using the SPIP™ software. The R_a values were 34.5, 9.6 and 8.7 nm for Zn–Ni, Zn–Co and Zn–Ni–Co, respectively. The Zn–Ni–Co coating exhibited the most uniform roughness distribution (based on Abbott–Firestone curves).

3.6. The surface morphology of coatings

The ESEM images in Fig. 4a,b,c reveal the typical surface morphologies of optimized Zn–Ni, Zn–Co and Zn–Ni–Co coatings. These coatings contained 3.8 wt% Ni, 1.7 wt% Co, and 14.4 wt.% Ni–6.4 wt% Co, respectively. In all cases the coatings seemed fairly uniform and did not contain surface mud-cracks. The Zn–Ni coating (Fig. 4a) shows dendritic growth that indicates on a mass transport-controlled electrocrystallization process. The Zn–Co coating (Fig. 4b) also exhibits dendritic growth, but with branches arranged in a pyramidal-like form. The surface morphology of the Zn–Ni–Co coating (Fig. 4c) was much different and consisted of bars with rectangular cross-section. This granular coating may be associated with higher concentrations of Ni and Co in the deposit.

3.7. The surface chemistry of coatings

XPS measurements were made. Fig. 5 presents selected spectra of zinc before and after sputter cleaning. It is difficult to discriminate between non-oxidized zinc and oxidized zinc because the Zn $2p_{3/2}$ spectra are similar for both states (1021.6 eV and 1021.7 eV, respectively) [30]. To overcome this problem, the Auger spectrum of Zn ($L_3M_{45}M_{45}$) was recorded and reported in Fig. 5. The chemical compositions after sputter cleaning are summarized in Table 5. Before sputter cleaning, the Zn–Ni alloy showed only C, O, Zn and N (in descending order) at the surface. The Zn–Co also showed these four elements only, in this descending order, but with slightly higher concentrations of Zn and O. The Zn–Ni–Co alloy again showed only these four elements at the surface, which was similar to Zn–Ni than to Zn–Co. After sputter cleaning (Table 5), N disappeared and C significantly reduced, as expected. In the case of the binary alloys, either Ni or Co appeared. In both cases, the concentration of oxygen was significantly lower than that in the ternary alloy. Thus, the latter may be oxidized even after sputter cleaning. In addition, the concentration of Zn was significantly lower in the ternary alloy compared to the binary alloys.

Fig. 5 shows that while zinc is present at the surface of the Zn–Ni coating before sputter cleaning in the oxidized (ZnO) state, in the bulk material it is present in the non-oxidized (Zn) state. The same behavior applies for Zn–Co. On the other hand, while zinc is present at the surface of the Zn–Ni–Co coating before sputter cleaning in the oxidized state too, in the bulk of this ternary alloy it exists both in the oxidized and in the non-oxidized states. Analysis of the Ni 2p and Co 2p peaks (not shown here) also indicated that they may be slightly oxidized in the bulk material. The O 1s peak (not shown here) seemed to consist of one component only, with a binding energy typical of ZnO. No evidence of $Zn(OH)_2$ at a higher binding energy was found.

3.8. The phase composition in the coatings

Fig. 6 shows the XRD patterns for Zn–Ni, Zn–Co and Zn–Ni–Co coatings on steel. Except of one reflection that could not be indexed (at around 75.4°), all reflections could be related either to iron (from

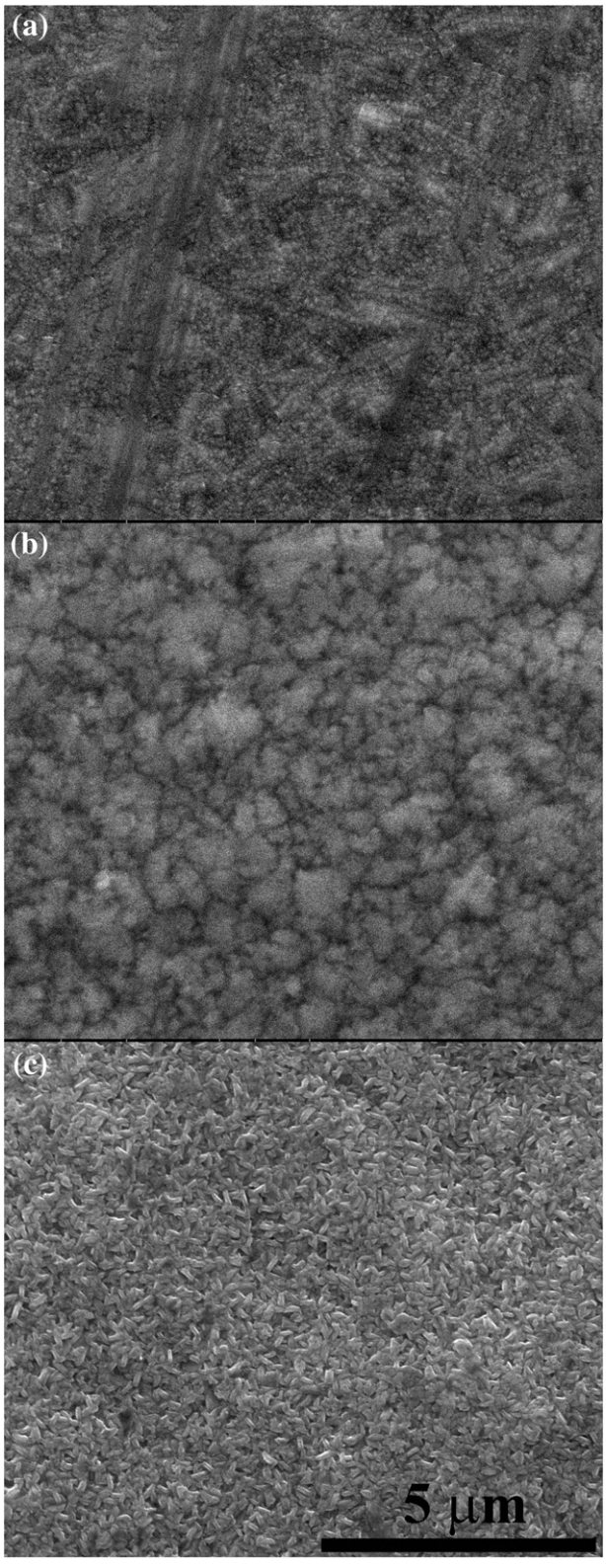

Fig. 4. ESEM images demonstrating the typical surface morphology of optimized (a) Zn–Ni ($i=30$ mA cm^{-2}), (b) Zn–Co ($i=20$ mA cm^{-2}), and (c) Zn–Ni–Co ($i=40$ mA cm^{-2}) coatings.

the steel substrate) or to the η and γ phases. This finding is supported by the cyclic voltammetry data (Section 3.1), according to which only these phases formed in baths containing both gelatin and SA. However, based on the interpretation of the anodic peaks in the cyclic voltammograms, it cannot be excluded that some of the peaks indexed as η are actually pure Zn. In the case of the Zn–Co coating, the more intense reflections from the iron substrate indicated a thinner coating, as also evident when comparing Table 2 with Table 3. The XRD pattern of the Zn–Ni–Co coating was different than that of the binary alloy coatings—the intensity of η(101) became the highest. This change in phase content may be responsible for the different appearance in ESEM images, as well as to different corrosion resistance (Fig. 4). It should be noted that, in contrast to the XPS data where zinc was found to exist in the bulk of the ternary alloy both in the oxidized and in the non-oxidized states, no match could be found in Fig. 6 to reflections typical of ZnO. This discrepancy could result from a small volume of the oxidized phase which is not detectable by XRD, or from the different sampling depths in both analytical techniques which results in different meanings of the terms 'surface' and 'bulk'. It could also be associated with the preferential sputtering phenomenon known to occur in XPS analysis.

3.9. Corrosion resistance

Data on the corrosion potential (E_{corr}), corrosion current density (i_{corr}) and corrosion rate (*CR*) of Zn–Ni, Zn–Co and Zn–Ni–Co alloys is summarized in Tables 2, 3 and 4, respectively. In the case of Zn–Ni alloys, the lowest corrosion rate (214 μm y^{-1}) characterized coatings deposited at $i=30$ mA cm^{-2}. The difference in the corrosion potentials of different coatings was maximum 79 mV. In the case of Zn–Co alloys, the lowest corrosion rate (138 μm y^{-1}) was attained for coatings deposited at $i=20$ mA cm^{-2}. The maximal difference between corrosion potentials reduced to 48 mV. The ternary alloy Zn–Ni–Co exhibited enhanced corrosion performance, with the lowest corrosion rate (20 μm y^{-1}) and most noble (less negative) corrosion potential for coatings deposited at $i=40$ mA cm^{-2}. In the case of the ternary alloy, the corrosion potential was most sensitive to the current density at which the coating was deposited. Following the discussion in Section 3.2 and Tables 2, 3 and 4, it is evident that the minimal corrosion rates neither corresponded to the highest content of the more noble element (iron-group metal) in the coating nor to the highest thickness of coating. The reason that coatings deposited at the highest current densities exhibited lower corrosion resistance is that they had higher level of porosity. Potentiodynamic polarization curves of the three alloy coatings deposited at their optimal current density are presented in Fig. 7. The highest corrosion potential of the Zn–Ni–Co alloy and the beginning of its passivity regime (at less negative potentials) are both evident. When comparing in Fig. 1 the area beneath the peaks in the anodic sweep in baths containing both gelatin and SA, it seemed that the η-to-γ content ratio was lower in the ternary alloy compared to the binary alloys. As sacrificial behavior has been related to the η phase while barrier behavior has been attributed to the γ phase [29], this could explain the lower corrosion rate of the ternary alloy.

EIS is a useful technique for ranking coatings, assessing interfacial reactions, quantifying coating breakdown, and predicting the lifetime of coating/metal systems. It has been used, for example, to monitor the underfilm corrosion of polymer-coated cobalt [55,56]. Fig. 8 shows the EIS Nyquist plots of the three alloys in 5% NaCl solution, where $Z'(\omega)$ and $Z''(\omega)$ are the real and imaginary parts of the measured impedance, respectively, and ω is the angular frequency. The inset provides a zoon-in of the plots at the high-frequency range as well as the suggested equivalent circuit (obtained with the aid of the ZSimpWin 3.21 software). Here, R_s is the solution resistance, C_c is the capacitance of the coating, R_{po} is the resistance of the porous layer, R_{ct} is the charge transfer resistance, and C_{dl} is the double layer capacitance. The solution resistance was nearly identical in all cases as the same bath chemistry and cell configuration were used. Reasonably good agreement was obtained between the measured and fitted spectra, supporting the ladder model in the inset of Fig. 8. The measured Nyquist plots reveal two relaxation processes, one in the high- and one in the low-frequency

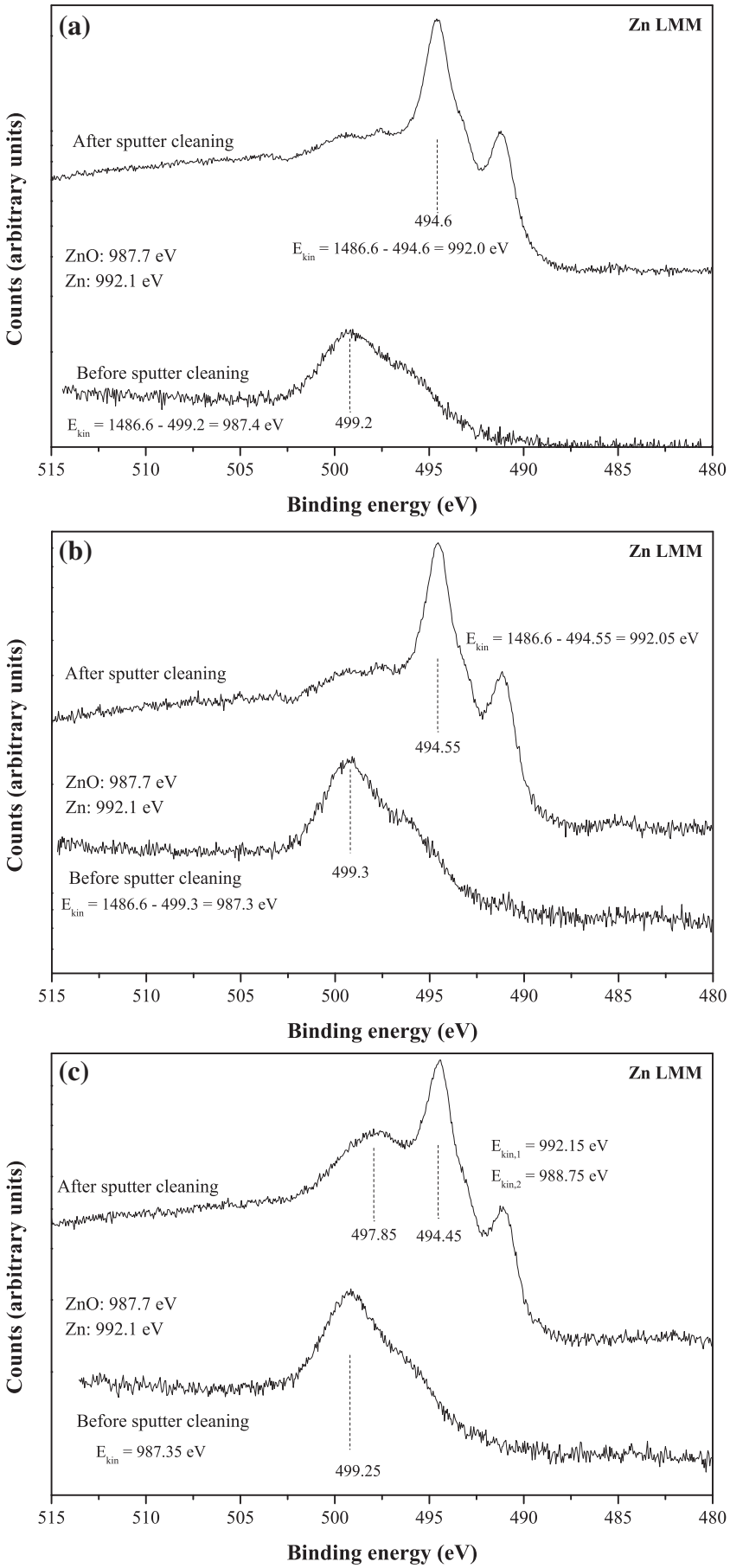

Fig. 5. XPS spectra showing the Zn LMM peak before and after sputter cleaning for: (a) Zn–Ni ($i = 30$ mA cm^{-2}), (b) Zn–Co ($i = 20$ mA cm^{-2}), and (c) Zn–Ni–Co ($i = 40$ mA cm^{-2}).

Table 5
Atomic concentration of elements (%) after sputter cleaning.

	Zn–Ni	Zn–Co	Zn–Ni–Co
Zn	79.84	77.39	67.50
Ni	9.18	–	6.88
Co	–	9.66	3.87
O	8.69	10.21	20.25
C	2.29	2.74	1.50

range. It is well known that the capacitance of oxide layers is typically very low, and their impedance response usually appears in the high-frequency range. The high-frequency time constant could thus be attributed to the formation of a porous oxide layer (corrosion product), while the low-frequency time constant should be related to the activation process itself. The significantly higher impedance and larger diameter of (unfinished) semicircle in the case of the ternary alloy reflect its higher corrosion resistance, which can be related to a change in the coating capacitance. The capacitive impedance at high frequencies is well related to the thickness and the dielectric constant of the coating. The decrease in this constant for the Zn–Ni–Co alloy reflected its higher corrosion resistance. No diffusion-limited process, in the form of Warburg impedance, was evident.

The slope of the Mott–Schottky plot (not shown herein) for the ternary alloys was much higher than the corresponding slopes of the lines for the binary Zn–Ni and Zn–Co alloys (5.84×10^8, 1.87×10^5 and $2.48\times10^5 F^{-2} V^{-1}$, respectively). This also implies that the corrosion protection of Zn–Ni–Co is higher than that of Zn–Ni or Zn–Co and should result from some sort of synergistic effect of the two iron-group metals. The positive slope of the $1/C^2$ versus E plot, where C is the space-charge capacitance and E is the applied potential, may indicate that the surface film behaves like an n-type semiconductor, as suggested by Hong et al. [57] in an attempt to explain the corrosion behavior of pure Ti versus Ti–Ag alloy.

Different factors have been reported to determine the corrosion resistance of Zn–Ni, Zn–Co and Zn–Ni–Co coatings [4,5,9,15,17,25,27]. The codeposition of Co and Ni was effective in changing the phase content as well as the crystal orientation and producing finer grain size, which synergistically provided better corrosion resistance [25]. In the present study too, the Zn–Ni–Co alloy was found to differ in composition, phase content, crystal orientation and surface morphology compared to the binary Zn–Ni and Zn–Co alloys. These factors, together with a more protective characteristic of the surface oxide film, are probably responsible for the enhanced corrosion performance of the ternary alloy. However, more work is required in order to identify which factor is most important.

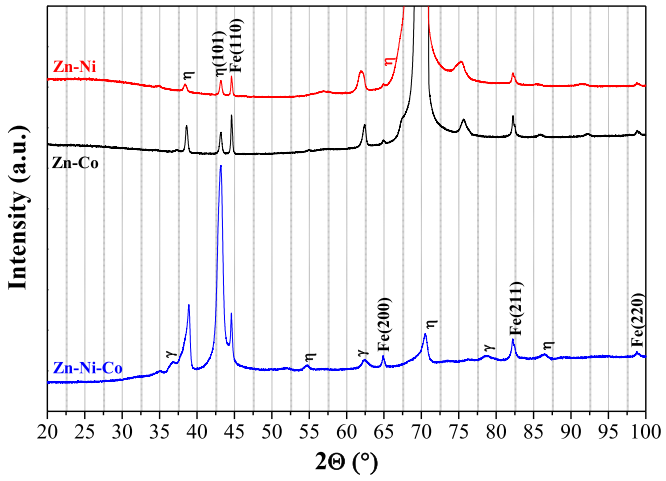

Fig. 6. XRD patterns typical of Zn–Ni ($i=30$ mA cm^{-2}), Zn–Co ($i=20$ mA cm^{-2}) and Zn–Ni–Co ($i=40$ mA cm^{-2}) coatings on steel.

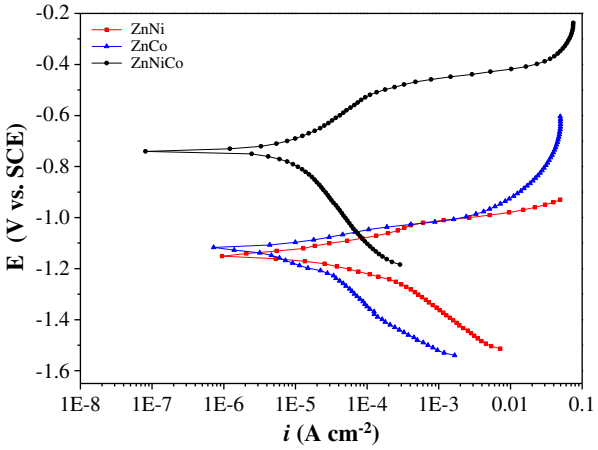

Fig. 7. Potentiodynamic polarization curves of Zn–Ni, Zn–Co and Zn–Ni–Co coatings, each deposited at its optimal current density. Scan rate: 1.0 mV s^{-1}.

4. Conclusions

Zn–Ni, Zn–Co and Zn–Ni–Co coatings were electrodeposited on mild steel from an acidic chloride bath containing sulphanilic acid (SA) and gelatin. The effects of bath composition, applied current density and bath temperature on the Faradaic efficiency, partial deposition current densities as well as on the coating's composition, hardness and thickness were studied. It was concluded that:

(1) In all cases the Faradaic efficiency was higher than 90%.
(2) As the applied current density was increased or the bath temperature was decreased, the concentration of the nobler (iron-group) metal in the coating increased.
(3) Both concentrations of Ni and Co in the ternary alloy increased as the applied current density was increased. Comparing between the Zn–Ni and Zn–Co systems, at each current density the concentration of Ni in the coating was higher than that of Co. This may be attributed to the higher concentration of the former ion in solution.
(4) For each current density, the concentrations of Ni and Co in the ternary alloy were higher than their corresponding concentrations in the binary alloys. Hence, nickel and cobalt had a synergistic catalytic effect.
(5) The thickness of all coatings increased as the applied current density was increased. The Zn–Ni coatings were thicker than the Zn–Co coatings.
(6) The hardness of the coating increased with current density to a peak value, and then decreased. The peak hardness of the Zn–Ni and Zn–Ni–Co alloys was similar, and slightly higher than that of Zn–Co.
(7) The rate of Zn deposition was heavily influenced by mass-transport limitation at high applied current densities, while the rates of Ni and Co deposition were not.
(8) The composition of the coating was most likely governed by adsorption of gelatin and SA on the surface of the cathode. The effect of gelatin was more pronounced than that of SA in the bath containing these two additives.
(9) The high concentrations of the less noble metal (Zn) in the coatings reflect anomalous codeposition (ACD) in all three systems. The best model to explain this behavior is based on the great difference between the exchange current densities of Zn and the iron-group metals (the former being much greater).
(10) Potentiodynamic polarization scans and electrochemical impedance spectroscopy (EIS) showed that the corrosion rate of the ternary Zn–Ni–Co alloy coatings was approximately 10 times lower in 5% NaCl at 25 °C than that of Zn–Ni and 7 times

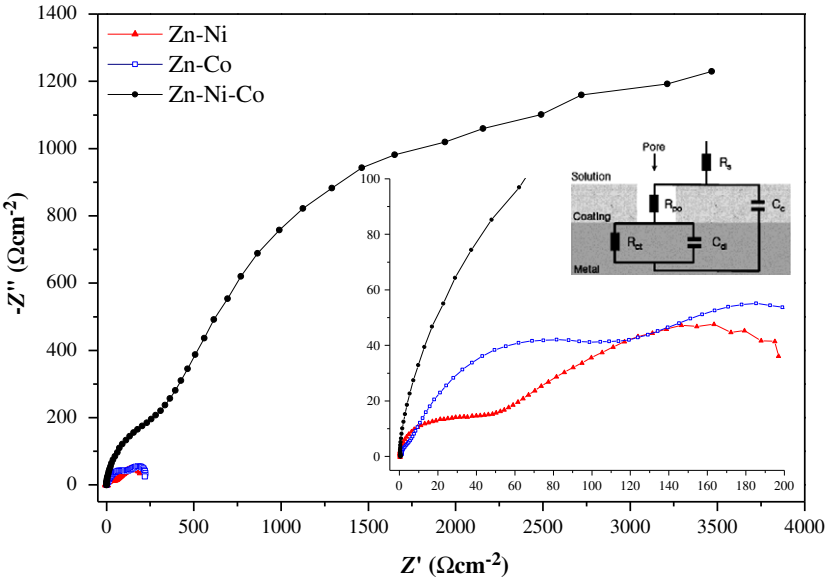

Fig. 8. EIS Nyquist spectra of Zn–Ni, Zn–Co and Zn–Ni–Co coatings, each deposited at its optimal processing parameters. The inset shows the high-frequency range at higher magnification as well as the proposed equivalent circuit.

lower than that of Zn–Co. The corrosion potential of the ternary alloy was less negative. For electrodeposition at pH = 3.5 and $T = 30$ °C, applied deposition current densities of 20, 30 and 40 mA cm^{-2} resulted in the highest corrosion resistance of Zn–Co, Zn–Ni and Zn–Ni–Co coatings, respectively. The improved corrosion resistance of the ternary alloy was attributed to its unique surface chemistry (e.g. significantly higher oxygen content), phase content and orientation, homogeneity, surface morphology and reduced roughness, as well as to the change in the intrinsic electrical properties of the surface film.

Acknowledgements

The authors thank Mario Levinstein from the Biomaterials and Corrosion Lab for his machinery and AFM work. We also thank Zahava Barkay, Larisa Burstein and Yuri Rosenberg from the Wolfson Applied Materials Research Center for their ESEM/EDS, XPS and XRD analyses, respectively. We are grateful to Eliezer Gileadi for his comments and useful ideas.

References

[1] N. Eliaz, E. Gileadi, in: C.G. Vayenas (Ed.), Modern Aspects of Electrochemistry, Vol. 42, Springer, New York, 2008, p. 191.
[2] R. Fratesi, G. Roventi, G. Giuliani, C.R. Tomachuk, J. Appl. Electrochem. 27 (1997) 1088.
[3] Z.L. Wang, Y.X. Yang, Y.R. Chen, J. Corros. Sci. Eng. 7 (2005) 18.
[4] A.B. Velichenko, J. Portillo, X. Alcobé, M. Sarret, C. Müller, Electrochim. Acta 46 (2000) 407.
[5] T.V. Byk, T.V. Gaevskaya, L.S. Tsybulskaya, Surf. Coat. Technol. 202 (2008) 5817.
[6] M.S. Chandrasekar, S. Srinivasan, M. Pushpavanam, J. Solid State Electrochem. 13 (2009) 781.
[7] R. Ramanauskas, R. Juškėnas, A. Kaliničenko, L.F. Garfias-Mesias, J. Solid State Electrochem. 8 (2004) 416.
[8] M. Sider, C. Fan, D.L. Piron, J. Appl. Electrochem. 31 (2001) 313.
[9] M.E. Soares, C.A.C. Souza, S.E. Kuri, Surf. Coat. Technol. 201 (2006) 2953.
[10] D.E. Hall, Plat. Surf. Finish. 70 (1983) 59.
[11] Bruet-Hotellaz, J.P. Bonino, A. Rousset, Marolleau, E. Chauveau, J. Mater. Sci. 34 (1999) 881.
[12] I.G. Bobrikova, F.I. Kukoz, V.N. Selivanov, A.V. Kopin, Russ. J. Electrochem. 38 (2002) 1148.
[13] A.V. Petrauskas, L.S. Grintsyavichene, Prot. Met. 37 (2001) 580.
[14] G.Y. Li, J.S. Lian, L.Y. Niu, Z.H. Jiang, Surf. Coat. Technol. 191 (2005) 59.
[15] R. Ramanauskas, L. Gudavičiūtė, A. Kaliničenko, R. Juškėnas, J. Solid State Electrochem. 9 (2005) 900.
[16] I. Ivanov, I. Kirilova, J. Appl. Electrochem. 33 (2003) 239.
[17] J.B. Bajat, S. Stanković, B.M. Jokić, J. Solid State Electrochem. 13 (2009) 755.
[18] J. Mahieu, K. De Wit, B.C. De Cooman, A. De Boeck, J. Mater. Eng. Perform. 8 (1999) 561.
[19] J.Y. Fei, G.D. Wilcox, Electrochim. Acta 50 (2005) 2693.
[20] M.E. Bahrololoom, D.R. Gabe, G.D. Wilcox, J. Electrochem. Soc. 150 (2003) C144.
[21] V. Thangaraj, N. Eliaz, A.C. Hegde, J. Appl. Electrochem. 39 (2009) 339.
[22] L. Felloni, R. Fratesi, E. Quadrini, G. Roventi, J. Appl. Electrochem. 17 (1987) 574.
[23] R. Albalat, E. Gómez, C. Müller, M. Sarret, E. Vallés, J. Pregonas, J. Appl. Electrochem. 20 (1990) 635.
[24] M.M. Younan, T. Oki, J. Appl. Electrochem. 26 (1996) 537.
[25] M.M. Younan, J. Appl. Electrochem. 30 (2000) 55.
[26] H. Bai, F. Wang, J. Mater. Sci. Technol. 23 (2007) 4.
[27] M.M. Abou-Krisha, H.M. Rageh, E.A. Matter, Surf. Coat. Technol. 202 (2008) 3739.
[28] A. Brenner, Electrodeposition of Alloys, Vol. II, Academic Press, New York, 1963.
[29] S. Swathirajan, J. Electrochem. Soc. 133 (1986) 671.
[30] S. Lichušina, A. Chodosovskaja, A. Sudavičious, R. Juškėnas, D. Bučinskienė, A. Selskis, E. Juzeliūnas, CHEMIJA 19 (2008) 25.
[31] J.L. Ortiz-Aparicio, Y. Meas, G. Trejo, R. Ortega, T.W. Chapman, E. Chainet, P. Ozil, Electrochim. Acta 52 (2007) 4742.
[32] K. Higashi, H. Fukushima, T. Urakawa, T. Adaniya, K. Matsudo, J. Electrochem. Soc. 128 (1981) 2081.
[33] H. Yan, J. Downes, P.J. Boden, S.J. Harris, J. Electrochem. Soc. 143 (1996) 1577.
[34] M.F. Mathias, T.W. Chapman, J. Electrochem. Soc. 134 (1987) 1408.
[35] E. Gómez, E. Vallés, J. Electroanal. Chem. 397 (1995) 177.
[36] F.J. Fabri Miranda, O.E. Barcia, S.L. Diaz, O.R. Mattos, R. Wiart, Electrochim. Acta 41 (1996) 1041.
[37] R. Valotkienė, K. Leinartas, D. Virbalytė, E. Juzeliūnas, CHEMIJA 12 (2001) 236.
[38] N. Eliaz, T.M. Sridhar, E. Gileadi, Electrochim. Acta 50 (2005) 2893.
[39] T.M. Sridhar, N. Eliaz, E. Gileadi, Electrochem. Solid-State Lett. 8 (2005) C58.
[40] A. Naor, N. Eliaz, E. Gileadi, Electrochim. Acta 54 (2009) 6028.
[41] A. Naor, N. Eliaz, E. Gileadi, J. Electrochem. Soc. 157 (2010) D422.
[42] K. Boto, Electrodep. Surf. Treat. 3 (1975) 77.
[43] A.I. Vogel, Quantitative Inorganic Analysis, Longmans Green and Co, London, 1951, p. 456.
[44] P. Díaz-Arista, Y. Meas, R. Ortega, G. Trejo, J. Appl. Electrochem. 35 (2005) 217.
[45] G. Trejo, R. Ortega, Y. Meas, E. Chainet, P. Ozil, J. Appl. Electrochem. 33 (2003) 373.
[46] B. Szczygieł, A. Laszczyńska, W. Tylus, Surf. Coat. Technol. 204 (2010) 1438.
[47] A. Petrauskas, L. Grincevičienė, A. Češūnienė, R. Juškėnas, Electrochim. Acta 50 (2005) 1189.
[48] S. Swathirajan, J. Electroanal. Chem. 221 (1987) 211.
[49] G. Trejo, H. Ruiz, R. Ortega Borges, Y. Meas, J. Appl. Electrochem. 31 (2001) 685.
[50] E. Gómez, X. Alcobe, E. Vallés, J. Electroanal. Chem. 505 (2001) 54.
[51] K.R. Baldwin, C.J.E. Smith, M.J. Robinson, Trans. Inst. Met. Finish. 72 (1994) 79.
[52] I. Rodriguez-Torres, G. Valentin, F. Lapicque, J. Appl. Electrochem. 29 (1999) 1035.
[53] S.S.A. El Rehim, E.E. Fouad, S.M.E. El Wahab, H.H. Hassan, Electrochim. Acta 41 (1996) 1413.
[54] S. Chandra, Comprehensive Inorganic Chemistry, Vol. II, New Age International Publishers, New Delhi, 2006, p. 132.
[55] N.J. Cantini, D.B. Mitton, N. Eliaz, G. Leisk, S.L. Wallace, F. Bellucci, G.E. Thompson, R.M. Latanision, Electrochem. Solid-State Lett. 3 (2000) 275.
[56] D.B. Mitton, S.L. Wallace, N.J. Cantini, F. Bellucci, G.E. Thompson, N. Eliaz, R.M. Latanision, J. Electrochem. Soc. 149 (2002) B265.
[57] S.B. Hong, N. Eliaz, E.M. Sachs, S.M. Allen, R.M. Latanision, Corros. Sci. 43 (2001) 1781.